

Kalman-Filter-Based Integration of IMU and UWB for High-Accuracy Indoor Positioning and Navigation

Daquan Feng¹, Chunqi Wang, Chunlong He¹, *Member, IEEE*, Yuan Zhuang², *Member, IEEE*, and Xiang-Gen Xia, *Fellow, IEEE*

Abstract—The emerging Internet of Things (IoT) applications, such as smart manufacturing and smart home, lead to a huge demand on the provisioning of low-cost and high-accuracy positioning and navigation solutions. Inertial measurement unit (IMU) can provide an accurate inertial navigation solution in a short time but its positioning error increases fast with time due to the cumulative error of accelerometer measurement. On the other hand, ultrawideband (UWB) positioning and navigation accuracy will be affected by the actual environment and may lead to uncertain jumps even under line-of-sight (LOS) conditions. Therefore, it is hard to use a standalone positioning and navigation system to achieve high accuracy in indoor environments. In this article, we propose an integrated indoor positioning system (IPS) combining IMU and UWB through the extended Kalman filter (EKF) and unscented Kalman filter (UKF) to improve the robustness and accuracy. We also discuss the relationship between the geometric distribution of the base stations (BSs) and the dilution of precision (DOP) to reasonably deploy the BSs. The simulation results show that the prior information provided by IMU can significantly suppress the observation error of UWB. It is also shown that the integrated positioning and navigation accuracy of IPS significantly improves that of the least squares (LSs) algorithm, which only depends on UWB measurements. Moreover, the proposed algorithm has high computational efficiency and can realize real-time computation on general embedded devices. In addition, two random motion approximation model algorithms are proposed and evaluated in the real environment. The experimental results show that the two algorithms can achieve certain robustness and continuous tracking ability in the actual IPS.

Index Terms—Extended Kalman filter (EKF), indoor positioning system (IPS), inertial measurement unit (IMU), Internet of Things (IoT), ultrawideband (UWB), unscented Kalman filter (UKF).

I. INTRODUCTION

LOW-COST and high-accuracy positioning and navigation solutions for indoor mobile robots have become critical in the Internet of Things (IoT) applications, such as smart manufacturing and smart home [1]. The inertial navigation system (INS) is based on kinematics and Newton classical mechanics [2]. The core of the INS is the inertial measurement unit (IMU), which consists of a three-axis accelerometer and a three-axis gyroscope [3], [4]. The IMU can obtain the attitude information and motion characteristics of the carrier, such as acceleration, angular velocity, and angle [5]. Without using any reference base stations (BSs), the position of the carrier can be directly calculated by mathematical integrations of acceleration. Because of its low cost, low environmental impact and high accuracy in a short time period, INS has been widely used in mobile object positioning and navigation scenarios, such as aircrafts, vehicles, and pedestrians, but errors increase rapidly with time [6]. On the other hand, many researchers have considered to adopt the ultrawideband (UWB) technology in the indoor positioning system (IPS) [7] and lots of work has been done, including channel model [8], multipath component estimation [9], and theoretical lower band of positioning errors [10]. UWB is a communication technology that uses nanosecond nonsinusoidal narrow pulse signal to transmit data, it has become an effective transmission technology in location-aware sensor networks [11]. Inherently, the UWB-based ranging technology has the advantages of short pulse interval and high time resolution and can achieve centimeter-level ranging accuracy [12]. In addition, it has good robustness to against the multipath effect [13]. However, due to the high frequency band of UWB, it is only suitable for line-of-sight (LOS) conditions. When there exist opaque objects, the ranging accuracy will be greatly reduced. Therefore, if only IMU or UWB is used, it is difficult to achieve high accuracy in complex indoor environments. To this end, the researcher has considered to take advantages of their complementary characteristics to improve the positioning and navigation accuracy [14]. A multisensor fusion architecture

Manuscript received August 2, 2019; revised November 11, 2019 and December 9, 2019; accepted December 25, 2019. Date of publication January 9, 2020; date of current version April 14, 2020. This work was supported in part by the National Natural Science Foundation of China under Grant 61701317, in part by the Young Elite Scientists Sponsorship Program by CAST under Grant 2018QNRC001, in part by the Guangdong Natural Science Foundation under Grant 2017A030310371, in part by the Shenzhen Overseas High-Level Talents Innovation and Entrepreneurship under Grant KQJSCX20180328093835762, in part by the Tencent Rhinoceros Birds-Scientific Research Foundation for Young Teachers of Shenzhen University, in part by the Natural Science Foundation of SZU, and in part by the Start-up Fund of Peacock Project. (*Corresponding author: Chunlong He.*)

Daquan Feng, Chunqi Wang, and Chunlong He are with the Guangdong Province Engineering Laboratory for Digital Creative Technology and Guangdong Key Laboratory of Intelligent Information Processing, Shenzhen University, Shenzhen 518060, China (e-mail: fdquan@gmail.com; chunlonghe@163.com).

Yuan Zhuang is with the State Key Laboratory of Information Engineering in Surveying, Mapping and Remote Sensing, Wuhan University, Wuhan 430079, China.

Xiang-Gen Xia is with the College of Electronics and Information Engineering, Shenzhen University, Shenzhen 518060, China, and also with the Department of Electrical and Computer Engineering, University of Delaware, Newark, DE 19716 USA.

Digital Object Identifier 10.1109/IIOT.2020.2965115

is proposed for the IPS in [15]. When UWB is available and reliable, the long-term drift error of IMU is calibrated by UWB. Otherwise, the system will switch from UWB to IMU immediately to get the positioning and navigation status. In [16], an integrated positioning solution of IMU and UWB is proposed, which can provide reliable and continuous position, especially in the case of non-LOS (NLOS) conditions. However, in [16], to address the time synchronization issue, all the UWB modules are connected to a central controller via the fiber line. This will increase the complexity of the deployment and the cost of the system. Both [15] and [16] use the time of arrival (TOA) ranging algorithm and have not considered the clock drift effect. Moreover, although the acceleration noise from IMU is considered in the acceleration measurements, the effect of acceleration noise on the velocity and displacement due to the integration is not considered in [15] and [16]. In [17], a drift-free and real-time localization and tracking algorithm combining IMU, UWB and region-specific sensor is proposed. It is shown that the fusion algorithm can obtain more accurate 3-D velocity and height information by using the lower body biomechanical model. Similarly, a magnetometer-free lower body motion capture (MOCAP) algorithm is introduced in [18], where it combines IMU with the UWB positioning system and the human lower body biomechanical model for 3-D positioning and attitude tracking. Note that most of the existing indoor positioning and navigation systems are based on the human lower body MOCAP system [19], which increases the cost and deployment difficulty. Moreover, although the drift error in yaw angle estimation can be eliminated by the usage of the magnetometer in [20], it limits the applications under the long-standing magnetic interference in the indoor environment.

Therefore, to achieve low cost and high accuracy of the indoor positioning and navigation system, this article focuses on the integration of IMU and UWB based on Kalman filter (KF) algorithms. The data obtained by IMU are used for the state equation while the data obtained by UWB are used for the observation equation of KF. In UWB ranging, to better solve the clock synchronization and clock drift problems, we propose an enhanced asymmetric double-sided two-way ranging (EADS-TWR) algorithm. Specifically, in order to further improve the indoor positioning accuracy and reduce the deployment cost of BSs, the extended KF (EKF) algorithm and unscented KF (UKF) algorithm based on three BSs and single BS are adopted in our scheme, respectively. In addition, to reduce the jitter of positioning data, two approximate motion models, namely, approximate uniform motion (AUM) and approximate uniform acceleration motion (AUAM), are proposed to make the positioning results smoother and more stable. Considering that the positioning accuracy is not only affected by the distance measurement accuracy but also by the geometric distribution of the BS, we discuss the influence of the geometric distribution of BSs and the dilution of precision (DOP) on the positioning accuracy.

The main contributions of this article can be summarized as follows.

- 1) We propose a direct positioning algorithm (DPA) based on EKF fusion for single BS with single distance

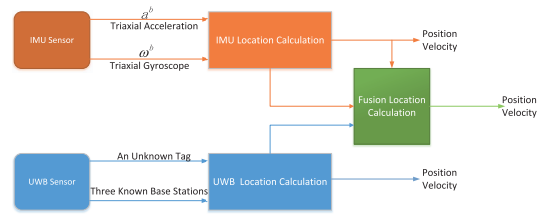


Fig. 1. System architecture of IMU and UWB integration.

and angle measurement. Compared with the traditional three BSs least squares (LSs) positioning algorithm, the proposed algorithm can greatly reduce the complexity and cost of BS deployment when the positioning accuracy requirement is not high.

- 2) UKF fusion positioning algorithm based on single BS and three BSs are proposed to reduce the computational complexity. The simulation results show that the UKF fusion algorithm can achieve better positioning accuracy than the EKF fusion positioning algorithm.
- 3) AUAM and AUM approximate motion models are proposed, which can greatly reduce the jitter of positioning data. The experimental results show that the positioning trajectories of the two models are smoother, and the performance of AUM is better than that of AUAM.

In Section II, the basic principles of IPS based on IMU and UWB are described. In Section III, the framework and algorithm of the integrated positioning system based on IMU and UWB are proposed. In Section IV, simulation and experimental results are presented and positioning performances of different algorithms are compared and discussed. In Section V, some conclusions are given.

II. POSITIONING AND NAVIGATION SYSTEM BASED ON THE INTEGRATION OF IMU AND UWB

In this section, we first describe the architecture of the indoor positioning and navigation system based on the integration of IMU and UWB, and then introduce the IMU-based and UWB-based positioning algorithms.

Fig. 1 describes the architecture of an indoor positioning and navigation system based on the integration of IMU and UWB. The IMU sensor consists of a three-axis accelerometer and a three-axis gyroscope. The UWB sensors consist of an unknown position tag and three BSs with known positions.

A. Positioning Processing Algorithms Based on IMU

Much work has been done on the transformations of different coordinate systems and the update calculation of the attitude matrix in strapdown INS (SINS) [21]. This article mainly introduces the basic principles, common coordinate systems, and related coordinate transformation matrix theory. The main principle of the SINS is shown in Fig. 2.

To describe the space motion state of the carrier well, it is necessary to choose an appropriate coordinate system. Assume that the body coordinate system (the B system) is represented by $Ox_b y_b z_b$ and the navigation coordinate system

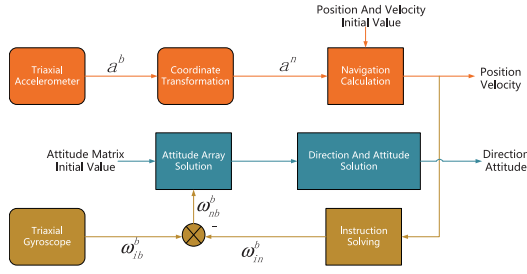


Fig. 2. Principle of SINS.

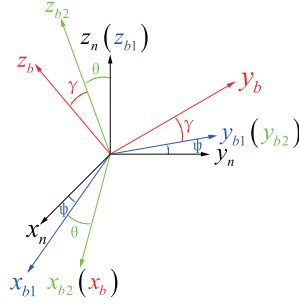


Fig. 3. Determination of carrier space angle position.

(the N system) is represented by $Ox_n y_n z_n$ as shown in Fig. 3. The origin coincides with the center of mass of the carrier. In the B system, the x_b -axis and y_b -axis point to the front along the longitudinal direction and the right along the transverse direction, respectively, and the z_b -axis is vertical along the carrier and forms the right-hand coordinate system with the x_b -axis and y_b -axis. In the N system, the east–north–down (END) coordinate system is selected. Specifically, the x_n -axis and the y_n -axis refer to the east and north directions in the local horizontal plane, respectively, and the z_n -axis points to the down along the vertical line of the earth to form the right-hand system. The coordinate transformation matrix between the B system and the N system is the attitude matrix of the carrier. The coordinates of the accelerometer and gyroscope in the system belong to the B system. The final output of acceleration, velocity, and position belong to the N system. Note that both Euler angle and quaternion methods can be used for the attitude updating in our IPS. However, considering that the Euler angle method is more intuitive and easy to understand than the quaternion method, we adopt the Euler angle method for the attitude transformation between the N system and the B system. Taking the N system as the reference coordinate system. The heading angle of the carrier is Yaw (expressed in ψ), the pitch angle is Pitch (expressed in θ), and the roll angle is Roll (expressed in γ). The parameters ψ , θ , and γ are a set of Euler angles, which describe the carrier space angular position relationship between the N system and the B system as shown in Fig. 3. When coordinates are rotated with Euler angles, the product of matrices cannot be exchanged since different products represent different rotation orders. The transformation matrix is the multiplication of the transformation matrices determined by the basic rotations which will be mathematically shown in detail below. The sequence of the multiplication is arranged from right to left in the order of the basic rotations.

Let C_n^1 , C_1^2 , and C_2^b denote the basic rotations from the N system to the first rotation system, from the first rotation system to the second rotation system and from the second rotational system to the B system, respectively. Then, the coordinate transformation matrix from the N system to the B system, C_n^b , is expressed as follows:

$$C_n^b = C_2^b C_1^2 C_n^1 \quad (1)$$

$$C_2^b = \begin{bmatrix} 1 & 0 & 0 \\ 0 & \cos \gamma & \sin \gamma \\ 0 & -\sin \gamma & \cos \gamma \end{bmatrix} \quad (2)$$

$$C_1^2 = \begin{bmatrix} \cos \theta & 0 & -\sin \theta \\ 0 & 1 & 0 \\ \sin \theta & 0 & \cos \theta \end{bmatrix} \quad (3)$$

$$C_n^1 = \begin{bmatrix} \cos \psi & \sin \psi & 0 \\ -\sin \psi & \cos \psi & 0 \\ 0 & 0 & 1 \end{bmatrix}. \quad (4)$$

On the other hand, the transformation matrix between two Cartesian coordinate systems is an orthogonal matrix. Thus

$$C_b^n = (C_n^b)^{-1} = (C_n^b)^T \quad (5)$$

$$C_b^n = \begin{bmatrix} \cos \psi \cos \theta & C_{12} & C_{13} \\ \cos \theta \sin \psi & C_{22} & C_{23} \\ -\sin \theta & \sin \gamma \cos \theta & \cos \theta \cos \gamma \end{bmatrix} \quad (6)$$

where C_b^n is the coordinate transformation matrix from the B system to the N system and

$$C_{12} = \sin \gamma \sin \theta \cos \psi - \cos \gamma \sin \psi$$

$$C_{13} = \sin \gamma \sin \psi + \cos \gamma \sin \theta \cos \psi$$

$$C_{22} = \cos \psi \sin \gamma + \sin \gamma \sin \theta \sin \psi$$

$$C_{23} = \sin \psi \sin \theta \cos \gamma - \sin \gamma \cos \psi.$$

In the system, attitude updating refers to the real-time calculation of matrix C_b^n based on the output of IMU. Let ω_{nb} denote the angular velocity of the B system relative to the N system. Then, the components of ω_{nb} in the B system, ω_{nb}^b , is given as follows:

$$\begin{bmatrix} \omega_{nbx}^b \\ \omega_{nby}^b \\ \omega_{nbz}^b \end{bmatrix} = C_2^b C_1^2 \begin{bmatrix} 0 \\ 0 \\ -\psi \end{bmatrix} + C_2^b \begin{bmatrix} 0 \\ \theta \\ 0 \end{bmatrix} + \begin{bmatrix} \gamma \\ 0 \\ 0 \end{bmatrix}. \quad (7)$$

Then, by expanding and merging, the Euler angle differential equation is obtained as follows:

$$\begin{bmatrix} \gamma \\ \theta \\ \psi \end{bmatrix} = \begin{bmatrix} 1 & 0 & -\sin \theta \\ 0 & \cos \gamma & \sin \gamma \cos \theta \\ 0 & -\sin \gamma & \cos \gamma \cos \theta \end{bmatrix}^{-1} \begin{bmatrix} \omega_{nbx}^b \\ \omega_{nby}^b \\ \omega_{nbz}^b \end{bmatrix}. \quad (8)$$

The acceleration in the B system, a^b , is measured by the three-axis accelerometer

$$a^b = [a_x^b \ a_y^b \ a_z^b]^T. \quad (9)$$

Thus, the acceleration in the N system, a^{n1} , is obtained by the coordinate transformation

$$a^{n1} = [a_x^{n1} \ a_y^{n1} \ a_z^{n1}]^T = C_n^b a^b. \quad (10)$$

If the gravity vector g is removed from the acceleration of the N system, then the acceleration in the N system, a^n , is obtained

$$a^n = \begin{bmatrix} a_x^n \\ a_y^n \\ a_z^n \end{bmatrix} = \begin{bmatrix} a_x^{n1} \\ a_y^{n1} \\ a_z^{n1} \end{bmatrix} - \begin{bmatrix} 0 \\ 0 \\ g \end{bmatrix}. \quad (11)$$

When the sample interval is short, the carrier is approximately subjected to constant force and with uniform acceleration of linear motion. Let Δv^n denote the velocity variation in the N system. Then, by substituting Newton's second law for momentum conservation equation, we have

$$\begin{bmatrix} \Delta v_x^n \\ \Delta v_y^n \\ \Delta v_z^n \end{bmatrix} = \begin{bmatrix} a_x^n \\ a_y^n \\ a_z^n \end{bmatrix} \Delta t. \quad (12)$$

Let $v^n(t)$ denote the velocity in the N system at time t . Then, the velocity in the N system at time $t + 1$, $v^n(t + 1)$, can be obtained by the acceleration integral as follows:

$$\begin{bmatrix} v_x^n(t + 1) \\ v_y^n(t + 1) \\ v_z^n(t + 1) \end{bmatrix} = \begin{bmatrix} v_x^n(t) \\ v_y^n(t) \\ v_z^n(t) \end{bmatrix} + \begin{bmatrix} \Delta v_x^n \\ \Delta v_y^n \\ \Delta v_z^n \end{bmatrix}. \quad (13)$$

Let $\Delta \chi^n$ denote the displacement variation in the N system. Then

$$\begin{bmatrix} \Delta \chi_x^n \\ \Delta \chi_y^n \\ \Delta \chi_z^n \end{bmatrix} = \begin{bmatrix} v_x^n \\ v_y^n \\ v_z^n \end{bmatrix} \Delta t + \frac{1}{2} \begin{bmatrix} a_x^n \\ a_y^n \\ a_z^n \end{bmatrix} \Delta t^2. \quad (14)$$

Let $\chi^n(t)$ denote the position in the N system at time t , and then the position in the N system at time $t + 1$, $\chi^n(t + 1)$, is described as follows:

$$\begin{bmatrix} \chi_x^n(t + 1) \\ \chi_y^n(t + 1) \\ \chi_z^n(t + 1) \end{bmatrix} = \begin{bmatrix} \chi_x^n(t) \\ \chi_y^n(t) \\ \chi_z^n(t) \end{bmatrix} + \begin{bmatrix} \Delta \chi_x^n \\ \Delta \chi_y^n \\ \Delta \chi_z^n \end{bmatrix}. \quad (15)$$

B. Positioning Processing Algorithm Based on UWB

The wireless signal-based positioning methods are generally divided into the ranging-based and nonranging-based methods. The UWB positioning method usually adopts the ranging-based algorithm and has two steps. The first step is to measure the distance and angle information, and the second step is to calculate the position using the measurement distance and angle information.

Time of flight (TOF) ranging is the common method to measure the distance between two nodes. Most existing works in TOF adopt the symmetric double-sided two-way ranging (SDS-TWR) technology [22] and as shown in Fig. 4(a) to mitigate the influence of clock synchronization between nodes. However, the frequency drift caused by the crystal clock drift cannot be solved. Besides, the SDS-TWR technology requires a long processing time [23]. To overcome the above problems, we propose an improved EADS-TWR optimization algorithm in our model as shown in Fig. 4(b).

Define T_{prop} as the TOF between device A and device B, T_{roundA} as the time duration from device A sending the polling message to receiving the response message from device B, T_{roundB} as the time from device B sending the response message to receiving the final message from device A, and

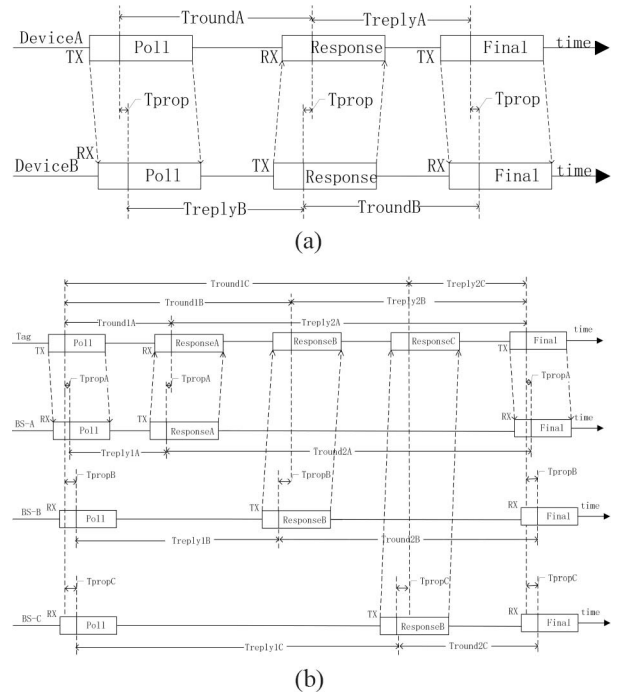


Fig. 4. Double-sided two way ranging protocol. (a) SDS-TWR protocol. (b) EADS-TWR protocol.

T_{replyA} and T_{replyB} as the time delay of devices A and B, respectively. Then, according to Fig. 4(b), it is easy to see that T_{roundA} and T_{roundB} can be expressed as follows:

$$\begin{aligned} T_{\text{roundA}} &= 2T_{\text{prop}} + T_{\text{replyB}} \\ T_{\text{roundB}} &= 2T_{\text{prop}} + T_{\text{replyA}}. \end{aligned} \quad (16)$$

Thus, we can get the TOF between devices A and B as follows:

$$T_{\text{prop}} = \frac{T_{\text{roundA}} \times T_{\text{roundB}} - T_{\text{replyA}} \times T_{\text{replyB}}}{T_{\text{roundA}} + T_{\text{roundB}} + T_{\text{replyA}} + T_{\text{replyB}}}. \quad (17)$$

Then, distance d can be expressed as

$$d = cT_{\text{prop}} \quad (18)$$

where c is the propagation velocity of the electromagnetic wave.

After completing the ranging process, we adopt the multi-lateration to determine the position of the tag based on the distance measurements. Specifically, Fig. 5 shows an example of trilateration, where the distances from the tag to three BSs are measured. Obviously, in the 2-D plane, the tag should be located at the intersection of three circles centered on three BSs. As long as the three BSs are not in a straight line, the result of the trilateration is unique.

Assuming that the unknown tag is located at (x, y) and the i th BS is located at (x_i, y_i) . Then, the true distance between the unknown tag and the i th BS, d_i , can be expressed as

$$d_i = \sqrt{(x_i - x)^2 + (y_i - y)^2}. \quad (19)$$

Let d'_i denote the measured distance between the unknown tag and the i th BS. Then, the difference between the true distance and the measured distance can be expressed as $\rho_i = d_i - d'_i$. To

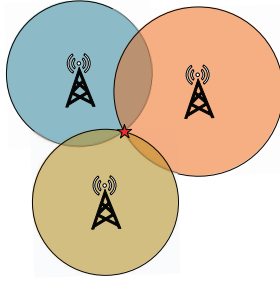


Fig. 5. LS position algorithm of three BSs.

deal with the ranging noise, we adopt the classic LS method to minimize the value of $\sum_{i=1}^n \rho_i^2$. Specifically, each distance determines an equation for the position of an unknown tag

$$\begin{cases} d_1^2 = (x_1 - x)^2 + (y_1 - y)^2 \\ d_2^2 = (x_2 - x)^2 + (y_2 - y)^2 \\ \vdots \\ d_n^2 = (x_n - x)^2 + (y_n - y)^2. \end{cases} \quad (20)$$

Let all the equations subtract the first equation, then we get

$$A\varepsilon = b \quad (21)$$

where

$$A = \begin{bmatrix} x_2 - x_1 & y_2 - y_1 \\ x_3 - x_1 & y_3 - y_1 \\ \vdots & \vdots \\ x_n - x_1 & y_n - y_1 \end{bmatrix}, \quad \varepsilon = \begin{bmatrix} x \\ y \end{bmatrix}$$

$$b = \frac{1}{2} \begin{bmatrix} x_2^2 + y_2^2 - d_2^2 - (x_1^2 + y_1^2 - d_1^2) \\ x_3^2 + y_3^2 - d_3^2 - (x_1^2 + y_1^2 - d_1^2) \\ \vdots \\ x_n^2 + y_n^2 - d_n^2 - (x_1^2 + y_1^2 - d_1^2) \end{bmatrix}. \quad (22)$$

Thus, the LS solution of ε is

$$\varepsilon = (A^T A)^{-1} A^T b. \quad (23)$$

In the LS method, each ranging value has adopted the same weight. Obviously, in the process of ranging, when the carrier is closer to the BS, the ranging error is smaller. Therefore, we choose a larger weight for the smaller ranging value, the positioning accuracy will be further improved. To this end, we propose the weighted LSs (WLSs) algorithm to solve the problem, in which the weighting coefficient η is expressed by the reciprocal of the ranging value d as

$$\eta = \begin{bmatrix} \frac{1}{d_2} & 0 & 0 & 0 \\ 0 & \frac{1}{d_3} & 0 & 0 \\ \vdots & \vdots & \ddots & \vdots \\ 0 & 0 & 0 & \frac{1}{d_n} \end{bmatrix}. \quad (24)$$

Then, the WLS solution of $\hat{\varepsilon}$ is expressed as

$$\hat{\varepsilon} = (A^T \eta A)^{-1} A^T \eta b. \quad (25)$$

III. MULTISENSOR DATA FUSION ALGORITHM BASED ON IMU AND UWB

In this section, we first introduce the EKF fusion positioning algorithm according to three distance measurements. Then, we propose the UKF fusion positioning algorithm by only single distance and angle measurements. Finally, we develop two approximate motion models, namely, AUM and AUAM, to further reduce the jitter of positioning data.

In the SINS, the positioning error may increase rapidly with time due to the cumulative error of accelerometer measurement [24]. On the other hand, UWB can provide centimeter-level ranging and positioning accuracy. However, the UWB signal is vulnerable to the obstacles and only suitable for LOS conditions. To this end, we consider to improve the positioning accuracy of the carrier by using KF to merge the data from IMU and UWB sensors.

It is known that linear KF can derive the optimal carrier state under the condition of the linear Gaussian model, in which the noises of IMU and UWB sensors are independent with each other and both obey Gaussian distribution with zero mean and variances σ^2 . However, there always exist some degrees of nonlinearity in the actual system, such as the square relation and trigonometric function relation in the state equation or observation equation. To more accurately approximate the nonlinear systems, various filtering algorithms are adopted to deal with the nonlinear factors. In [25], a dual filter integration for microelectromechanical system (MEMS) sensors and WiFi fingerprints are proposed, where the EKF algorithm is used to obtain the smooth constrained fingerprints.

A. EKF Algorithm Based on Distance Measurements

In the 2-D plane, assume that the tag is moving in a straight line with uniform acceleration, define $X(k)$ as the state vector at time k , contains position, $x(k)$, velocity, $v(k)$, and acceleration, $a(k)$, which can be expressed as follows:

$$X(k) = [x_x(k) \quad x_y(k) \quad v_x(k) \quad v_y(k) \quad a_x(k) \quad a_y(k)]^T. \quad (26)$$

When the sample time period is T , $T\omega(k)$ denotes the process noise of acceleration, $(T^2/2)\omega(k)$ denotes the process noise of velocity and $(T^3/6)\omega(k)$ denotes the process noise of position due to the double integral of acceleration, according to the equation of uniform acceleration motion at time $k+1$. Thus, the state equation can be expressed as follows:

$$\begin{cases} x_x(k+1) = x_x(k) + v_x(k)T + \frac{1}{2}a_x(k)T^2 + \frac{T^3}{6}\omega_x(k) \\ x_y(k+1) = x_y(k) + v_y(k)T + \frac{1}{2}a_y(k)T^2 + \frac{T^3}{6}\omega_y(k) \\ v_x(k+1) = v_x(k) + a_x(k)T + \frac{T^2}{2}\omega_x(k) \\ v_y(k+1) = v_y(k) + a_y(k)T + \frac{T^2}{2}\omega_y(k) \\ a_x(k+1) = a_x(k) + T\omega_x(k) \\ a_y(k+1) = a_y(k) + T\omega_y(k). \end{cases} \quad (27)$$

Then, the state equation in matrix form is expressed as follows:

$$X(k+1) = FX(k) + GW(k) \quad (28)$$

where F denotes the state transition matrix, G denotes the noise driving matrix, $W(k) = [\omega_x(k) \ \omega_y(k)]^T$ denotes process noise vector with zero mean and covariance matrix $Q = \text{diag}(\sigma_{ax}^2, \sigma_{ay}^2)$ at time k

$$F = \begin{bmatrix} 1 & 0 & T & 0 & \frac{T^2}{2} & 0 \\ 0 & 1 & 0 & T & 0 & \frac{T^2}{2} \\ 0 & 0 & 1 & 0 & T & 0 \\ 0 & 0 & 0 & 1 & 0 & T \\ 0 & 0 & 0 & 0 & 1 & 0 \\ 0 & 0 & 0 & 0 & 0 & 1 \end{bmatrix}, \quad G = \begin{bmatrix} \frac{T^3}{6} & 0 \\ 0 & \frac{T^3}{6} \\ \frac{T^2}{2} & 0 \\ 0 & \frac{T^2}{2} \\ T & 0 \\ 0 & T \end{bmatrix}. \quad (29)$$

Let $Z(k)$ denote the observation vector, containing the true distance $d_i(k)$ with the observation noise $v_i(k)$ at time k . Then, the observation equation can be expressed as follows:

$$Z(k) = \begin{bmatrix} d_1(k) + v_1(k) \\ d_2(k) + v_2(k) \\ \vdots \\ d_n(k) + v_n(k) \end{bmatrix} = H(k)X(k) + V(k) \quad (30)$$

where $H(k)$ represents the observation matrix, and $V(k) = [v_1(k) \ v_2(k) \ \dots \ v_n(k)]^T$ represents the observation noise vector with zero mean and covariance matrix $R = \text{diag}(\sigma_{d1}^2, \sigma_{d2}^2, \dots, \sigma_{dn}^2)$ at time k . In addition, the detailed distance equation is shown as follows:

$$\begin{bmatrix} d_1(k) \\ d_2(k) \\ \vdots \\ d_n(k) \end{bmatrix} = \begin{bmatrix} \sqrt{(x_x(k) - x_1)^2 + (y_x(k) - y_1)^2} \\ \sqrt{(x_x(k) - x_2)^2 + (y_x(k) - y_2)^2} \\ \vdots \\ \sqrt{(x_x(k) - x_n)^2 + (y_x(k) - y_n)^2} \end{bmatrix}. \quad (31)$$

Since (31) is nonlinear, it needs to be linearized and the EKF algorithm can be adopted. At each time step, by taking the first-order Taylor expansion, the Jacobian matrix, $H(k)$, is obtained as

$$H(k) \triangleq \begin{bmatrix} \frac{\partial d_1(k)}{\partial x_x(k)} & \frac{\partial d_1(k)}{\partial y_x(k)} & 0 & 0 & 0 & 0 \\ \frac{\partial d_2(k)}{\partial x_x(k)} & \frac{\partial d_2(k)}{\partial y_x(k)} & 0 & 0 & 0 & 0 \\ \vdots & \vdots & \vdots & \vdots & \vdots & \vdots \\ \frac{\partial d_n(k)}{\partial x_x(k)} & \frac{\partial d_n(k)}{\partial y_x(k)} & 0 & 0 & 0 & 0 \end{bmatrix} \quad (32)$$

where

$$\begin{cases} \frac{\partial d_i(k)}{\partial x_x(k)} = \frac{x_x(k) - x_i}{\sqrt{(x_x(k) - x_i)^2 + (y_x(k) - y_i)^2}} \\ \frac{\partial d_i(k)}{\partial y_x(k)} = \frac{y_x(k) - y_i}{\sqrt{(x_x(k) - x_i)^2 + (y_x(k) - y_i)^2}} \end{cases}$$

The main idea of the EKF algorithm is to linearize the nonlinear state or observation equations by Taylor's expansion and retains its first-order approximation term. However, this procedure inevitably introduces the linearization errors. If the linearization assumption is not true, the performance of the EKF algorithm will degrade and diverge. In addition, it is not easy to calculate the Jacobian matrix, which increases the computational complexity of the algorithm. The detailed process of the EKF algorithm is shown in Algorithm 1.

Algorithm 1 EKF Algorithm

Initialize: State mean $U(0) = E[X(0)]$, state covariance matrix $P(0) = \text{var}[X(0)]$, I_n is $n \times n$ unit matrix.

1: Predict state.

$$\hat{X}(k|k-1) = FX(k-1)$$

2: Predict state covariance matrix.

$$P(k|k-1) = FP(k-1|k-1)F^T + GQG^T$$

3: Calculate Kalman filter gain.

$$K = P(k|k-1)H^T(k)[H(k)P(k|k-1)H^T(k) + R]^{-1}$$

4: Update state.

$$X(k|k) = \hat{X}(k|k-1) + K[Z(k) - Z(k|k-1)]$$

5: Update state covariance matrix.

$$P(k|k) = [I_n - KH(k)]P(k|k-1)$$

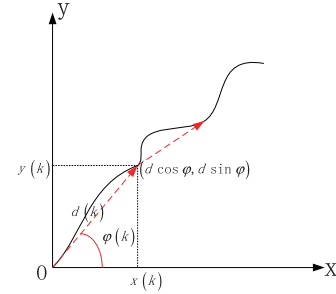


Fig. 6. DPA of single BS.

B. UKF Algorithm Based on Distance and Angle Measurements

Because of the EKF algorithm only uses the first-order approximation in the Taylor expansion, it inevitably introduces the linearization error. In the UKF algorithm, it does not use the linearization process of the nonlinear function. Particularly, for the one-step prediction, the mean and variance of the equation undergoing nonlinear transformation are captured by the unscented transformation (UT) [26]. The UKF algorithm approximates the probability density distribution of the nonlinear function. It obtains the posterior probability density of the state through a set of deterministic samples rather than approximating the nonlinear function by the derivative of the Jacobian matrix. In this way, it can effectively overcome the limitations of low accuracy and poor stability of the EKF algorithm.

In this article, to further reduce the deployment cost of the BSs, we propose an efficient positioning algorithm based on single BS with known position (x_0, y_0) . In particular, UWB detects distance d and angle φ between the tag and the BS to establish the observation equation, where the angle is obtained by applying the arctangent operation to the position difference. IMU detects the acceleration to establish the state equation. The single BS positioning process is shown in Fig. 6.

Assuming that the tag is moving in the 2-D plane with uniform acceleration, the state vector containing position, velocity, and acceleration is the same as that in the EKF

Algorithm 2 UKF Algorithm

Initialize: State mean $U_u(0) = E[X_u(0)]$, state covariance matrix $P_u(0) = \text{var}[X_u(0)]$.

1: Calculate sigma points.

$$X_u^{(i)}(k|k) = \begin{bmatrix} \bar{X}_u(k|k) \\ \bar{X}_u(k|k) + \sqrt{(n+\lambda)P_u(k|k)} \\ \bar{X}_u(k|k) - \sqrt{(n+\lambda)P_u(k|k)} \end{bmatrix}^T,$$

2: Predict sigma points.

$$\hat{X}_u^{(i)}(k+1|k) = FX_u^{(i)}(k|k), i = 1, \dots, 2n+1,$$

3: Calculate state mean and state covariance matrix.

$$\begin{aligned} \bar{X}_u(k+1|k) &= \sum_{i=0}^{2n} \omega_m^{(i)} \hat{X}_u^{(i)}(k+1|k), \\ P_u(k+1|k) &= \sum_{i=0}^{2n} \omega_c^{(i)} \left[\hat{X}_u^{(i)}(k+1|k) - \bar{X}_u(k+1|k) \right] \\ &\quad \left[\hat{X}_u^{(i)}(k+1|k) - \bar{X}_u(k+1|k) \right]^T + Q_u, \end{aligned}$$

4: Update sigma points.

$$X_u^{(i)}(k+1|k) = \begin{bmatrix} \bar{X}_u(k+1|k) \\ \bar{X}_u(k+1|k) + \sqrt{(n+\lambda)P_u(k+1|k)} \\ \bar{X}_u(k+1|k) - \sqrt{(n+\lambda)P_u(k+1|k)} \end{bmatrix}^T,$$

5: Predict observation.

$$\hat{Z}_u^{(i)}(k+1|k) = h(X_u^{(i)}(k+1|k)), i = 1, \dots, 2n+1,$$

6: Calculate observation mean and observation covariance matrix.

$$\begin{aligned} \bar{Z}_u(k+1|k) &= \sum_{i=0}^{2n} \omega_m^{(i)} \hat{Z}_u^{(i)}(k+1|k), \\ P_{z_k z_k} &= \sum_{i=0}^{2n} \omega_c^{(i)} \left[\hat{Z}_u^{(i)}(k+1|k) - \bar{Z}_u(k+1|k) \right] \\ &\quad \left[\hat{Z}_u^{(i)}(k+1|k) - \bar{Z}_u(k+1|k) \right]^T + R_u, \\ P_{x_k z_k} &= \sum_{i=0}^{2n} \omega_c^{(i)} \left[\hat{X}_u^{(i)}(k+1|k) - \bar{X}_u(k+1|k) \right] \\ &\quad \left[\hat{Z}_u^{(i)}(k+1|k) - \bar{Z}_u(k+1|k) \right]^T, \end{aligned}$$

7: Calculate Kalman gain matrix.

$$K = P_{x_k z_k} P_{z_k z_k}^{-1},$$

8: Update state and state covariance matrix.

$$\begin{aligned} X_u(k+1|k+1) &= \bar{X}_u(k+1|k) + K[Z_u(k+1) - \bar{Z}_u(k+1|k)], \\ P_u(k+1|k+1) &= P_u(k+1|k) - KP_{z_k z_k}K^T. \end{aligned}$$

algorithm as shown in (26) and (27). Then, the state equation in matrix form can be expressed as follows:

$$X_u(k+1) = FX_u(k) + W_u(k) \quad (33)$$

where F denotes the state transition matrix and is the same as that in (28) and (29) in the EKF algorithm, $W_u(k) = [\omega_{x_x}(k) \ \omega_{x_y}(k) \ \omega_{v_x}(k) \ \omega_{v_y}(k) \ \omega_{a_x}(k) \ \omega_{a_y}(k)]^T$ denotes the process noise vector with zero mean and covariance matrix $Q_u = \text{diag}(\sigma_{x_x}^2, \sigma_{x_y}^2, \sigma_{v_x}^2, \sigma_{v_y}^2, \sigma_{a_x}^2, \sigma_{a_y}^2)$.

Let $Z_u(k)$ denote the observation vector. It contains the true distance $d(k)$, true angle $\varphi(k)$ with observation distance noise $v_d(k)$, and observation angle noise $v_\varphi(k)$ at time k . Then, the

observation equation can be expressed as follows:

$$Z_u(k) = \begin{bmatrix} d(k) + v_d(k) \\ \varphi(k) + v_\varphi(k) \end{bmatrix} = h(X(k)) + V_u(k) \quad (34)$$

where $h(X(k))$ is a nonlinear function of the observation equation, and $V_u(k) = [v_d(k) \ v_\varphi(k)]^T$ is the observation noise vector with zero mean and covariance matrix $R_u = \text{diag}(\sigma_d^2, \sigma_\varphi^2)$

$$\begin{bmatrix} d(k) \\ \varphi(k) \end{bmatrix} = \begin{bmatrix} \sqrt{(x_x(k) - x_0)^2 + (x_y(k) - y_0)^2} \\ \arctan\left(\frac{x_y(k) - y_0}{x_x(k) - x_0}\right) \end{bmatrix}. \quad (35)$$

Unlike EKF, UKF does not need to compute the Jacobian matrix at each time and adopts UT to make the statistics keep consistent for the random variables undergoing nonlinear transformation [27]. For the Gaussian distribution, through carefully selecting the sample points, UT can capture the mean and covariance accurately to the third order. The selection of sample points is based on the prior mean and covariance matrix. Define a nonlinear transformation $y = f(x)$, where the random variable x is n -dimensional with mean \bar{x} and covariance matrix P . Then, the statistical characteristics of y can be calculated by forming a matrix χ of $2n+1$ sigma points $\chi^{(i)}$ with the corresponding weight ω as follows:

$$\begin{cases} \chi^{(0)} = \bar{x} \\ \chi^{(i)} = \bar{x} + (\sqrt{(n+\lambda)P})_i, & i = 1, \dots, n \\ \chi^{(i)} = \bar{x} - (\sqrt{(n+\lambda)P})_i, & i = n+1, \dots, 2n \end{cases} \quad (36)$$

where $(\sqrt{P})_i$ represents the i th column of the square root of a matrix. The corresponding weights of these sample points are calculated as follows:

$$\begin{cases} \omega_m^{(0)} = \frac{\lambda}{n+\lambda} \\ \omega_c^{(0)} = \frac{\lambda}{n+\lambda} + (1 - \alpha^2 + \beta) \\ \omega_m^{(i)} = \omega_c^{(i)} = \frac{1}{2(n+\lambda)}, & i = 1, 2, \dots, 2n \end{cases} \quad (37)$$

where $\omega_m^{(i)}$ is the weight of mean and $\omega_c^{(i)}$ is the weight of covariance of the sigma points, the superscript i is the index of sample points, and $\lambda \triangleq \alpha^2(n+\kappa) - n$ is a scaling parameter to reduce the total prediction error. In practice, α is usually set to a small positive value to keep the mean of the sigma points around \bar{x} , κ is set to zero to ensure that matrix $(n+\lambda)P$ is a semipositive-definite matrix, and β is a nonnegative weight coefficient to incorporate the prior distribution of x . According to (36) and (37), we can get a set of sigma points $X_u^{(i)}(k|k)$, and then further predict them to get the state mean and state covariance matrix as $\bar{X}_u(k+1|k)$ and $P_u(k+1|k)$, respectively. Similarly, we can get the observation mean and observation covariance matrix as $\bar{Z}_u(k+1|k)$ and $P_{z_k z_k}$, respectively, and also the cross-covariance matrix as $P_{x_k z_k}$ between the state vector and the observation vector. Then, we can calculate the Kalman gain, K , and finally obtain the state and state covariance matrix updates as $X_u(k+1|k+1)$ and $P_u(k+1|k+1)$, respectively. The detailed process of UKF algorithm is shown in Algorithm 2.

C. Dilution of Precision Models

The positioning accuracy is not only affected by the distance measurement accuracy but also by the geometric distribution of the BS. The DOP represents the geometric distribution of tag and BSs, which plays an important role in the positioning accuracy. The DOP mainly includes the following parameters: geometric DOP (GDOP), position DOP (PDOP), horizontal DOP (HDOP), vertical DOP (VDOP), and time DOP (TDOP). This article focuses on the positioning of the tag in the 2-D plane. Under the same distance measurement accuracy, the smaller the HDOP, the higher the positioning accuracy. Therefore, it is important to arrange the BS distribution reasonably to reduce the HDOP value. In detail, the HDOP can be defined as

$$\text{HDOP} = \frac{\sqrt{\sigma_x^2 + \sigma_y^2}}{\sigma_d} \quad (38)$$

where σ_d is the standard deviation of distance measurement error, σ_x^2 and σ_y^2 are the variances of x -axis and y -axis, respectively. According to (19), the derivatives at the approximate position (x', y') can be given as follows:

$$\begin{bmatrix} d_1 - d'_1 \\ d_2 - d'_2 \\ \vdots \\ d_n - d'_n \end{bmatrix} = \begin{bmatrix} \frac{\partial d_1}{\partial x} & \frac{\partial d_1}{\partial y} \\ \frac{\partial d_2}{\partial x} & \frac{\partial d_2}{\partial y} \\ \vdots & \vdots \\ \frac{\partial d_n}{\partial x} & \frac{\partial d_n}{\partial y} \end{bmatrix} \begin{bmatrix} x - x' \\ y - y' \end{bmatrix} \quad (39)$$

where

$$\begin{cases} \frac{\partial d_i}{\partial x} = \frac{x_i - x'}{\sqrt{(x_i - x')^2 + (y_i - y')^2}} \\ \frac{\partial d_i}{\partial y} = \frac{y_i - y'}{\sqrt{(x_i - x')^2 + (y_i - y')^2}} \end{cases}$$

When $n \geq 3$, the LS method can be used to solve (39) and we get

$$C = (B^T B)^{-1} B^T D \quad (40)$$

where

$$D = \begin{bmatrix} d_1 - d'_1 \\ d_2 - d'_2 \\ \vdots \\ d_n - d'_n \end{bmatrix}, \quad B = \begin{bmatrix} \frac{\partial d_1}{\partial x} & \frac{\partial d_1}{\partial y} \\ \frac{\partial d_2}{\partial x} & \frac{\partial d_2}{\partial y} \\ \vdots & \vdots \\ \frac{\partial d_n}{\partial x} & \frac{\partial d_n}{\partial y} \end{bmatrix}, \quad C = \begin{bmatrix} x - x' \\ y - y' \end{bmatrix}.$$

The covariance matrix of distance error R is the same as that in the EKF algorithm. The positioning error covariance matrix Q_C caused by distance error can be expressed as follows:

$$\begin{aligned} Q_C &= (B^T R^{-1} B)^{-1} B^T R^{-1} \sigma_u^2 \\ &= (B^T B)^{-1} \sigma_u^2 \\ &= E \sigma_u^2 \end{aligned} \quad (41)$$

where $E = (B^T B)^{-1}$ is a symmetric matrix representing the influence of distance error on positioning error, σ_u^2 is the variance of user equivalent ranging error (UERE), and the smaller UERE means better positioning accuracy [28]. Let

$$E = \begin{bmatrix} E_{11} & E_{12} \\ E_{21} & E_{22} \end{bmatrix}. \quad (42)$$

Finally, we can get the $\text{HDOP} = \sqrt{E_{11} + E_{22}}$.

Algorithm 3 AUAM Filtering Algorithm

Initialize: UWB sample time period $t=0.02\text{s}$ (the rate of updates by the UWB is 50Hz), IMU sample time period $T=0.01\text{s}$ (the rate of updates by the IMU is 100Hz)

1: Measure the distance.

$$d = [d_1 \quad d_2 \quad \dots \quad d_n]$$

2: Calculate the LS position.

$$\varepsilon(k) = (A^T A)^{-1} A^T b$$

3: Calculate the differential velocity.

$$v(k) = \frac{\varepsilon(k) - \varepsilon(k-1)}{t}$$

4: Convert the acceleration coordinate system.

$$a^n = [a_x^n \quad a_y^n] = C_b^n a^b$$

5: Update the position state.

$$\varepsilon(k+1) = \varepsilon(k) + v(k)t + \frac{1}{2}a^n T^2$$

D. AUAM and AUM Approximate Motion Models

Since the motion of the tag is usually random, it is difficult to establish an accurate motion model. Therefore, we propose two approximate motion models in a short time period: 1) one is the AUAM model and 2) the other is the AUM model. Specifically, the AUAM model combines the position and the differential velocity information from the UWB as well as the acceleration information from the IMU. The whole procedure of the AUAM filtering algorithm is shown in Algorithm 3. Without considering the acceleration from the IMU sensor, the AUAM model will degenerate into the AUM model which only integrates the position and differential velocity information.

IV. SIMULATION AND EXPERIMENTAL RESULTS

In this section, we evaluate the performance of the proposed algorithm by simulation and experiment. First, we compare the EKF fusion positioning algorithm with the LS and WLS positioning algorithms. Then, we evaluate the performances of the UKF fusion algorithm and the DPA algorithm based on a single BS. In addition, we compare the performances of the proposed EKF and UKF algorithms. Finally, we carry out experiments in the laboratory to verify the actual effect of the proposed algorithms.

A. EKF Simulation Results

In the simulations, it is assumed that the tag moves in the xy plane with the initial position at $(0, 0)$, the initial horizontal and vertical velocities are both at 0.15 m/s , the initial horizontal and vertical accelerations are both at 0.002 m/s^2 , the sample time period $T = 1 \text{ s}$, and the total running time $N = 50 \text{ s}$.

Fig. 7 demonstrates the performances of the LS and the proposed EKF algorithms in terms of the positioning trajectory and error, where Q and R denote the process and observation noise variances, respectively. As shown in Fig. 7(a), the LS trajectory has oscillation and the larger the observation noise variance is, the larger the oscillation appears.

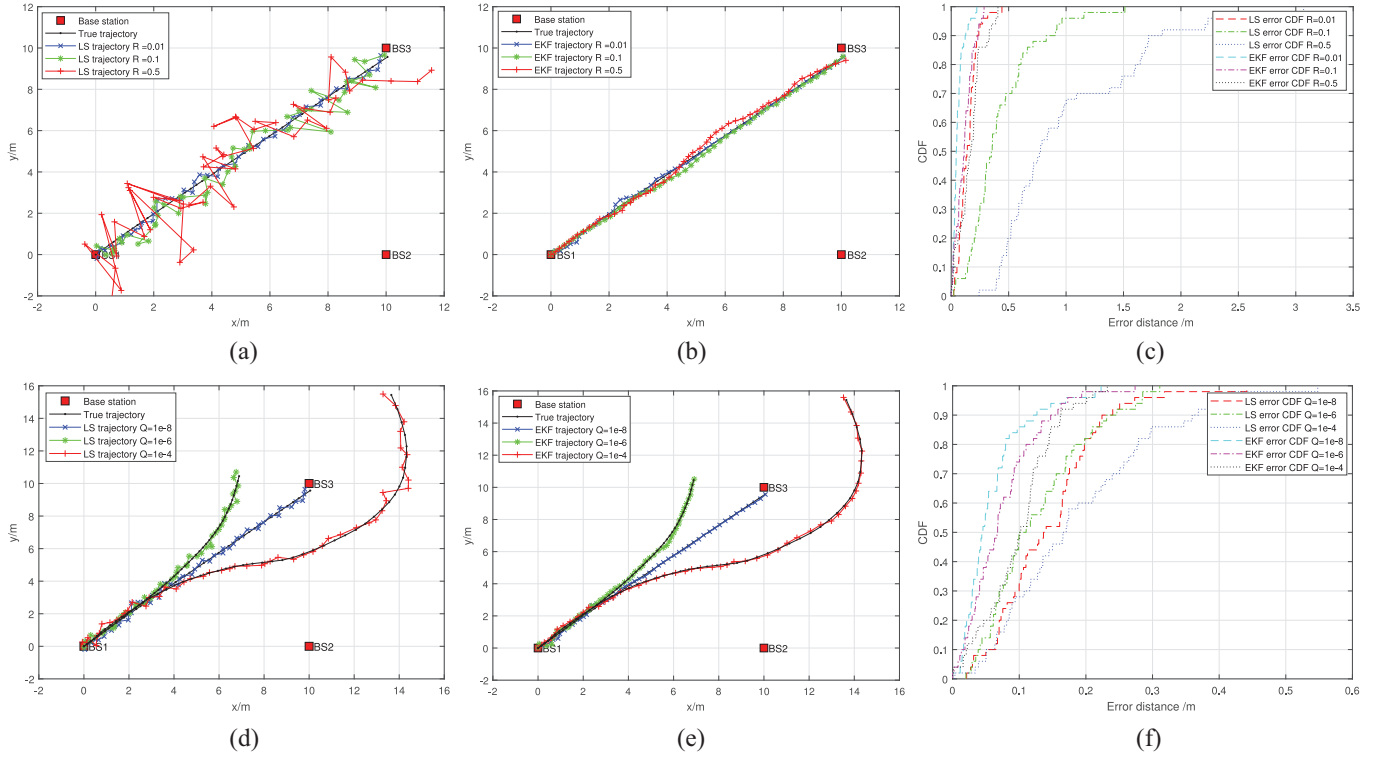


Fig. 7. Performances of LS and EKF algorithms. (a) LS trajectory ($Q = 10^{-8}$). (b) EKF trajectory ($Q = 10^{-8}$). (c) Position error CDF ($Q = 10^{-8}$). (d) LS trajectory ($R = 0.01$). (e) EKF trajectory ($R = 0.01$). (f) Position error CDF ($R = 0.01$).

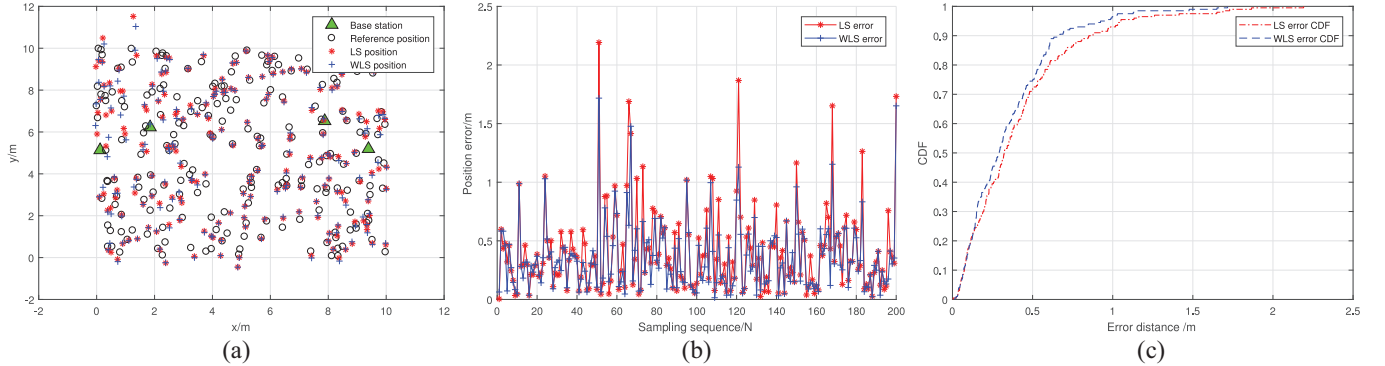


Fig. 8. Performances of LS and WLS algorithms. (a) LS and WLS position. (b) Position error. (c) Position error CDF.

It indicates that the observation noise has great influence on the measurements. However, after using the proposed EKF algorithm, the trajectory accuracy can be significantly improved and the results are much closer to the true trajectory as shown in Fig. 7(b). Moreover, it can be seen that when the observation noise variance increases, the EKF trajectory keeps consistent. As shown in Fig. 7(d), when the process noise variance becomes large, the carrier's motion will be curvilinear. However, after using the proposed EKF algorithm, the trajectory accuracy can be significantly improved and the results are much closer to the true trajectory as shown in Fig. 7(e). In Fig. 7(c) and (f), the cumulative distribution functions (CDF) of positioning errors are illustrated. Specifically, when $R = 0.01$ and $Q = 10^{-8}$, the maximum position error

of the LS algorithm is over 31 cm and the average position error is about 14 cm. For the proposed EKF algorithm, the maximum position error is about only 20 cm and the average position error is less than 9 cm. The positioning accuracy has been improved by about 50%. When $R = 0.01$ and $Q = 10^{-4}$, the maximum position error of the LS algorithm is over 57 cm and the average position error is about 18 cm. However, the maximum position error is about only 22 cm and the average position error is reduced to less than 10 cm when the proposed EKF fusion algorithm is used. In addition, to evaluate the performance of the WLS algorithm, we randomly generate four BSs with known positions and two hundred reference points on a 10-m by 10-m area. We also assume that the observation distance noise is white Gaussian noise with zero

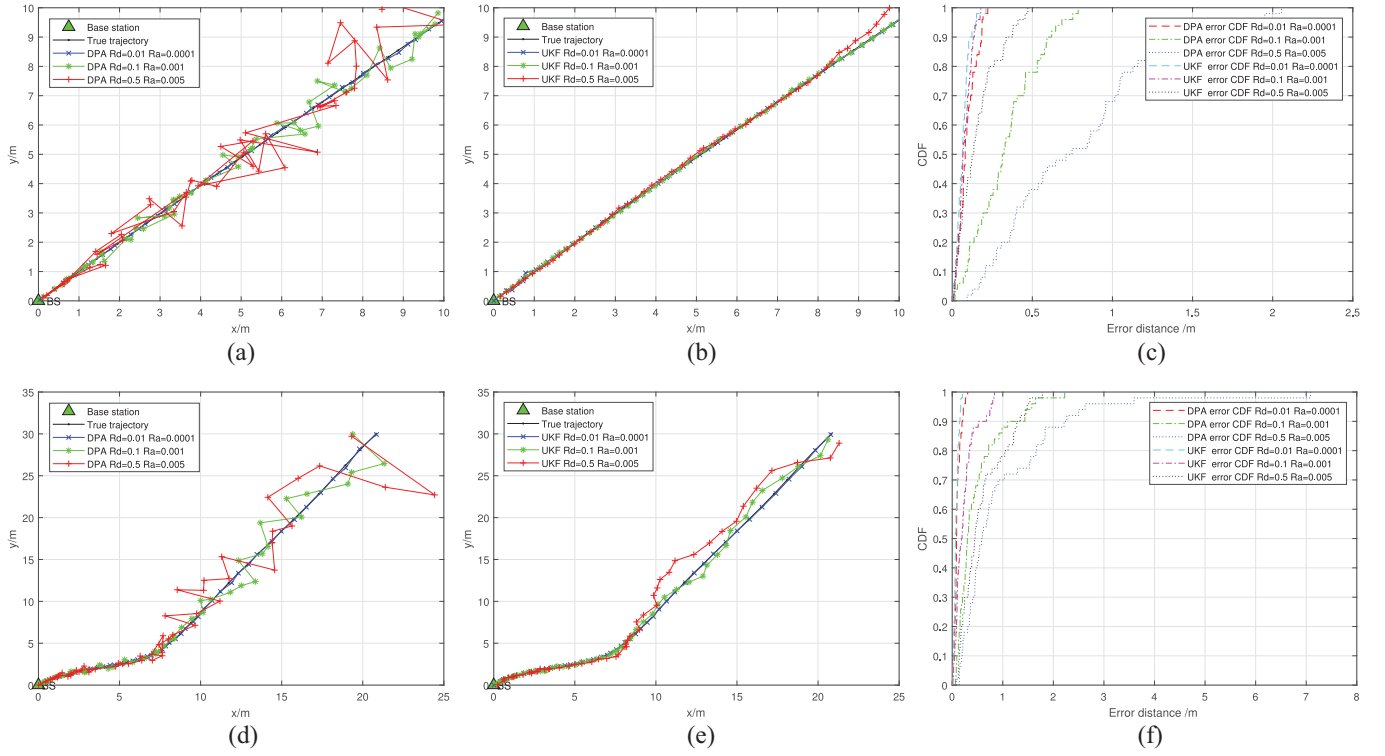


Fig. 9. Performances of DPA and UKF algorithms. (a) DPA trajectory ($Q = 10^{-8}$). (b) UKF trajectory ($Q = 10^{-8}$). (c) Position error CDF ($Q = 10^{-8}$). (d) DPA trajectory ($Q = 10^{-4}$). (e) UKF trajectory ($Q = 10^{-4}$). (f) Position error CDF ($Q = 10^{-4}$).

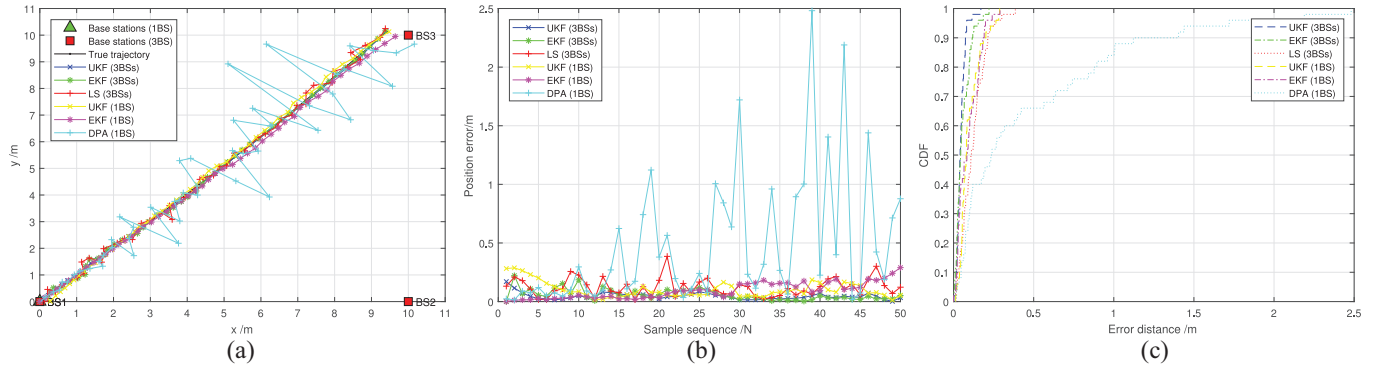


Fig. 10. Performances of EKF and UKF algorithms. (a) Position trajectory. (b) Position error. (c) Position error CDF.

mean and variance 0.01 m. The simulation results in Fig. 8 show that the positioning accuracy of the WLS algorithm is improved compared with the LS algorithm.

B. UKF Simulation Results

In the UKF simulations, it is also assumed that the tag moves in the xy plane with the initial position at (0, 0), the initial horizontal velocity and the vertical velocity are both at 0.15 m/s, the initial horizontal acceleration and the vertical acceleration are both at 0.002 m/s², the sample time period $T = 1$ s, and the total running time $N = 50$ s. The correlation coefficients $\alpha = 0.01$, $\beta = 2$, $\kappa = 0$, and state dimension $n = 6$, the observation dimension $m = 2$ in UT. In the following, R_d and R_a denote the observation distance noise variance and angle noise variance, respectively.

Fig. 9 compares the performances of the DPA without filtering and UKF algorithms. As shown in Fig. 9(a), at the initial stage, the DPA trajectory can continuously track the true trajectory. However, after several iterations, the oscillation appears. This is mainly due to the accumulation of observation angle noise. On the other hand, as shown in Fig. 9(b), the UKF trajectory can still track the true trajectory, which indicates that the proposed UKF algorithm can improve the positioning accuracy based on single observation distance and angle. Moreover, it is shown that when the observation noise variance increases, the UKF trajectory is still consistent with the true trajectory. Comparing Fig. 9(a) with Fig. 9(d) and Fig. 9(b) with Fig. 9(e), as the process noise becomes larger, the carrier's motion is to the curvilinear motion. In addition, the CDF of the positioning error is shown in Fig. 9(c) and (f). Specifically, when $R_d = 0.1$, $R_a = 0.001$, and $Q = 10^{-8}$, the

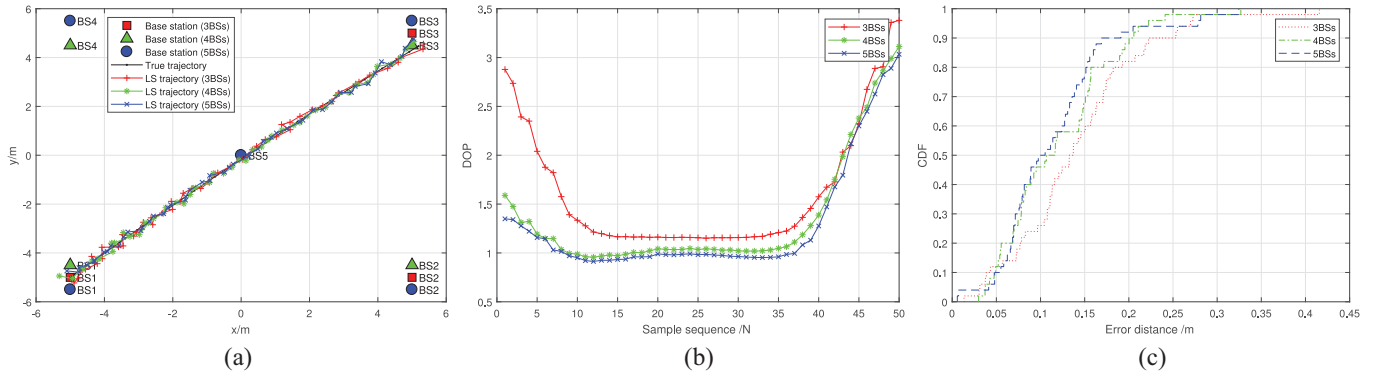


Fig. 11. DOP. (a) LS trajectory. (b) DOP results. (c) Position error CDF.

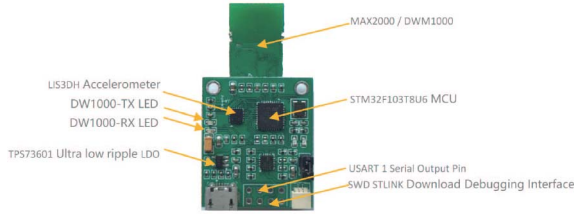


Fig. 12. Hardware architecture of the positioning module.

maximum position error of DPA is over 78 cm and the average position error is about 33 cm. However, for the proposed UKF algorithm, the maximum position error is about only 18 cm and the average position error is less than 7 cm. The positioning accuracy has been improved by about 78%. In order to better evaluate the performances of two positioning algorithms and two filtering algorithms, we compare their performances with the same assumption $R = 0.01$, $R_d = 0.01$, $R_a = 0.01$, and $Q = 10^{-8}$.

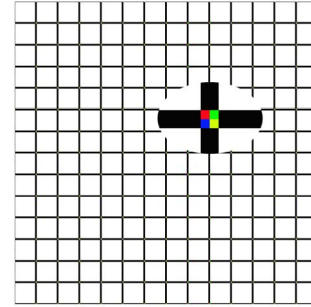
Fig. 10 shows the results of different positioning algorithms based on single BS and three BSs. The average positioning error of the LS algorithm based on three BSs is 15 cm, while that of the DPA algorithm based on single BS is 53 cm. The average positioning error of the EKF fusion algorithm based on three BSs is 6 cm, and that of a single BS is 18 cm. The average positioning error of the UKF fusion algorithm based on three BSs is 5 cm, and that of single BS is 13 cm. In summary, when the positioning accuracy requirement is high, multiple BS positioning algorithms can be selected, otherwise, single BS positioning algorithm can be selected to reduce the complexity and cost of deploying BSs.

C. DOP Simulation Results

In Fig. 11, we evaluate the influence of the distribution of BS. In the triangle model, the three BSs are located at $(-5, -5)$, $(5, -5)$, and $(5, 5)$; in square model, the four BSs are located at $(-5, -4.5)$, $(5, -4.5)$, $(5, 4.5)$, and $(-5, 4.5)$; in X model, the five BSs are located at $(-5, -5.5)$, $(5, -5.5)$, $(5, 5.5)$, $(-5, 5.5)$, and $(0, 0)$ as shown in Fig. 11(a). In Fig. 11(b), it can be seen that the HDOP value is relatively small in the center area and gradually increases outwards the edge of BSs. It is also shown that increasing the number of



(a)



(b)

Fig. 13. Indoor positioning and navigation experiment. (a) Experimental environment. (b) Ground grid.

BSs can reduce the HDOP value. However, the effect becomes less and less and it will increase the system complexity with the increase of BSs. The CDF result of the system positioning error is shown in Fig. 11(c).

D. Experiments and Results

The hardware used in this experiment is shown in Fig. 12, which is with the “baseplate and module” structure. The baseplate adopts STM32F103T8U6 microcomputer as the main control chip. The peripheral circuit includes power, LED indicator, lithium battery management, LIS3DH, accelerometer, etc. The modules are configured with DWM1000 of Decawave and MAX2000 of YCHIOT. Note that the hardware can be configured as BS or tag through the USB instruction.

The experimental environment is shown in Fig. 13(a), where each smaller grid on the ground is a square with a side length of 0.5 m. To accurately measure the true position of the tag, all the brackets and the BSs are deployed in the same way. Then, the true position of the tag is determined by the vertical

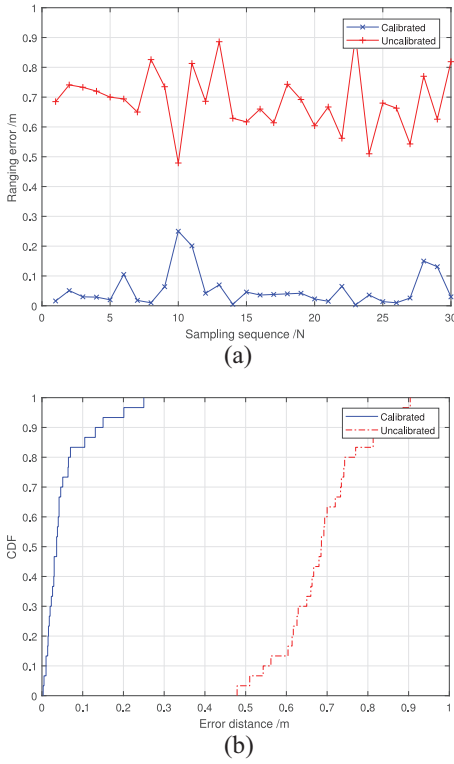


Fig. 14. Experiment of ranging calibration. (a) Calibration experiment. (b) Ranging error CDF.

projection of the center points of small red, green, blue, and yellow squares from the top of the module antenna to the ground grid, as shown in Fig. 13(b).

Since the actual ranging measurement is affected by the environment, including latitude, longitude, air quality, obstacle height, and other factors, we must first calibrate the module. Particularly, the calibration coefficients can be obtained by measuring the distance between BS and tag. There are many fitting formulas to fit the data and the simplest linear equation is used in the experiments. Obviously, the ranging accuracy will become better after calibrating as shown in Fig. 14.

In the first experiment scenario, the tag starts from (1, 1) and moves two rounds along a square with a side length of 4 m as shown in Fig. 15. The experimental results show that the LS trajectory oscillates relative to the true trajectory due to the influence of noise. The AUAM filtering trajectory has a good tracking effect in the initial stage, but the error caused by the acceleration becomes larger with the passage of time. The AUM filtering trajectory keeps continuous tracking. It can also be seen that the positioning trajectories of the AUAM and AUM algorithms are smoother than the LS algorithm.

In the second experiment scenario, the tag moves along a square with a side length of 6 m as shown in Fig. 16. In the spiral experiment, the results show that the root mean square error (RMSE) of x -axis is 7.79 cm, and that of y -axis is 6.32 cm. In the circuitous experiment, the results show that the RMSE of x -axis is 5.50 cm, and that of y -axis is 5.03 cm. It is because there are fewer sample points on the edge of the BSs in the circuitous experimental. Thus, when the tag is closer to the center, the positioning accuracy is better. It implies that

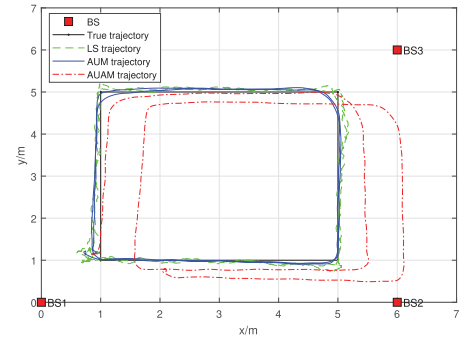


Fig. 15. Experiments of AUAM and AUM models.

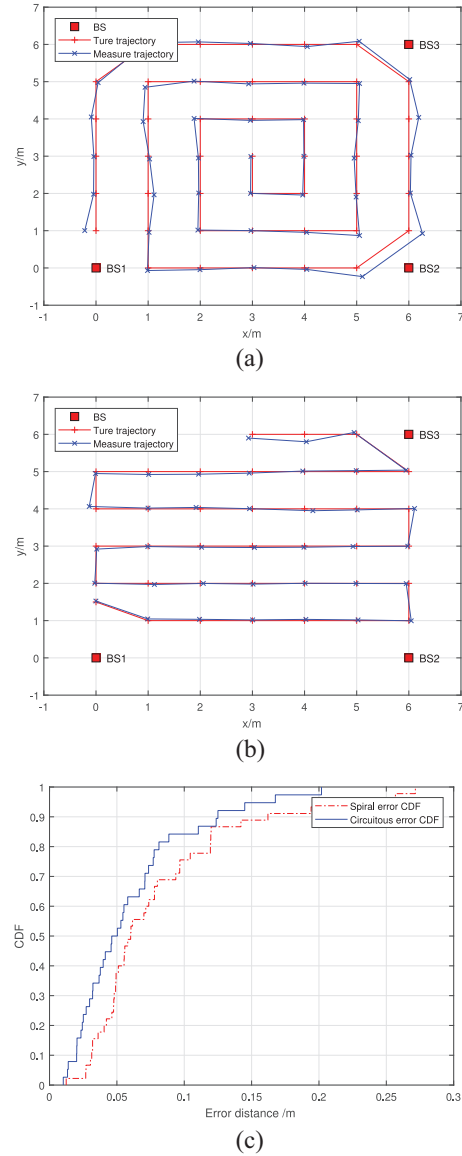


Fig. 16. Experiments of spiral and circuitous. (a) Experiments of spiral. (b) Experiments of circuitous. (c) Position error CDF.

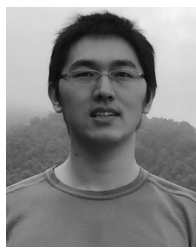
expanding the deployment of the BSs and ensuring that the tag always moves in the center of the coverage can effectively improve the positioning accuracy.

V. CONCLUSION

In this article, a fusion positioning system based on IMU and UWB was studied. The data obtained by IMU were used for the state equation of KF while the data obtained by UWB was used for the observation equation of KF. First, the EKF algorithm based on multiple observation BSs was introduced to improve the positioning accuracy. Then, an efficient UKF algorithm based on single observation BS was proposed to reduce the deployment complexity of BS and lower the cost. In addition, to reduce the jitter of positioning data, two approximate motion models, namely, AUM and AUAM, were proposed to make the positioning results smoother and more stable. In addition, the experimental results showed that the proposed EKF algorithm improves the positioning accuracy by 54% compared to the LS algorithm and the proposed UKF algorithm improves the positioning accuracy by 50% compared to the DPA algorithm. Note that in our system, we have only considered the Gaussian noise distribution. Thus, for reducing the complexity, we have only studied the EKF and UKF methods. In the future work, we will consider a generalized noise distribution, and focus on the application and the optimization of other filter methods, e.g., particle filter.

REFERENCES

- [1] Y. Zhuang, Q. Wang, M. Shi, P. Cao, L. Qi, and J. Yang, "Low-power centimeter-level localization for indoor mobile robots based on ensemble Kalman smoother using received signal strength," *IEEE Internet Things J.*, vol. 6, no. 4, pp. 6513–6522, Aug. 2019.
- [2] Y. Zhuang and N. El-Sheimy, "Tightly-coupled integration of WiFi and MEMS sensors on handheld devices for indoor pedestrian navigation," *IEEE Sensors J.*, vol. 16, no. 1, pp. 224–234, Jan. 2016.
- [3] Y. Li, Y. Zhuang, P. Zhang, H. Lan, X. Niu, and N. El-Sheimy, "An improved inertial/WiFi/magnetic fusion structure for indoor navigation," *Inf. Fusion*, vol. 34, pp. 101–119, Mar. 2017.
- [4] Y. Li, Z. He, Z. Gao, Y. Zhuang, C. Shi, and N. El-Sheimy, "Toward robust crowdsourcing-based localization: A fingerprinting accuracy indicator enhanced wireless/magnetic/inertial integration approach," *IEEE Internet Things J.*, vol. 6, no. 2, pp. 3585–3600, Apr. 2019.
- [5] Y. Zhuang, J. Yang, L. Qi, Y. Li, Y. Cao, and N. El-Sheimy, "A pervasive integration platform of low-cost MEMS sensors and wireless signals for indoor localization," *IEEE Internet Things J.*, vol. 5, no. 6, pp. 4616–4631, Dec. 2018.
- [6] C. Ren, Q. Liu, and T. Fu, "A novel self-calibration method for MIMU," *IEEE Sensors J.*, vol. 15, no. 10, pp. 5416–5422, Oct. 2015.
- [7] K. Guo *et al.*, "Ultra-wideband-based localization for quadcopter navigation," *Unmanned Syst.*, vol. 4, no. 1, pp. 23–24, Feb. 2016.
- [8] A. Chandra *et al.*, "Frequency-domain in-vehicle UWB channel modeling," *IEEE Trans. Veh. Technol.*, vol. 65, no. 6, pp. 3929–3940, Jun. 2016.
- [9] S. Wang, G. Mao, and J. A. Zhang, "Joint time of arrival estimation for coherent UWB ranging in multipath environment with multi user interference," *IEEE Trans. Signal Process.*, vol. 67, no. 14, pp. 3743–3755, Jul. 2019.
- [10] A. Alarifi *et al.*, "Ultra wideband indoor positioning technologies: Analysis and recent advances," *Sensors*, vol. 16, no. 5, p. 707, May 2016.
- [11] S. Marano, W. M. Gifford, H. Wymeersch, and M. Z. Win, "NLOS identification and mitigation for localization based on UWB experimental data," *IEEE J. Sel. Areas Commun.*, vol. 28, no. 7, pp. 1026–1035, Sep. 2010.
- [12] Y. Lu, J. Yi, L. He, X. Zhu, and P. Liu, "A hybrid fusion algorithm for integrated INS/UWB navigation and its application in vehicle platoon formation control," in *Proc. Int. Conf. Comput. Sci. Electron. Commun. Eng. (CSECE)*, Feb. 2018, pp. 157–161.
- [13] M. Gunia, F. Protze, N. Joram, and F. Ellinger, "Setting up an ultra-wideband positioning system using off-the-shelf components," in *Proc. IEEE 13th Workshop Position. Navig. Commun. (WPNC)*, Oct. 2016, pp. 1–6.
- [14] Y. Zhuang, Y. Cao, N. El-Sheimy, and J. Yang, "Guest editorial: Special issue on toward positioning, navigation, and location-based services (PNLBS) for Internet of Things," *IEEE Internet Things J.*, vol. 5, no. 6, pp. 4613–4615, Dec. 2018.
- [15] L. Yao, Y.-W. A. Wu, L. Yao, and Z. Liao, "An integrated IMU and UWB sensor based indoor positioning system," in *Proc. IEEE Int. Conf. Indoor Position. Indoor Navig. (IPIN)*, Sep. 2017, pp. 1–8.
- [16] Y. Zhong, T. Liu, B. Li, L. Yang, and L. Lou, "Integration of UWB and IMU for precise and continuous indoor positioning," in *Proc. IEEE Ubiquitous Position. Indoor Navig. Location Based Services (UPINLBS)*, Mar. 2018, pp. 1–5.
- [17] P. K. Yoon, S. Zihajehzadeh, B.-S. Kang, and E. J. Park, "Robust biomechanical model-based 3-D indoor localization and tracking method using UWB and IMU," *IEEE Sensors J.*, vol. 17, no. 4, pp. 1084–1096, Feb. 2017.
- [18] S. Zihajehzadeh and E. J. Park, "A novel biomechanical model-aided IMU/UWB fusion for magnetometer-free lower body motion capture," *IEEE Trans. Syst., Man, Cybern., Syst.*, vol. 47, no. 6, pp. 927–938, Jun. 2017.
- [19] S. Zihajehzadeh, P. K. Yoon, B. S. Kang, and E. J. Park, "UWB-aided inertial motion capture for lower body 3-D dynamic activity and trajectory tracking," *IEEE Trans. Instrum. Meas.*, vol. 64, no. 12, pp. 3577–3587, Dec. 2015.
- [20] T. Seel and S. Rupp, "Eliminating the effect of magnetic disturbances on the inclination estimates of inertial sensors," in *Proc. 20th IFAC World Congr.*, vol. 50, Jul. 2017, pp. 8798–8803.
- [21] L. Chang, J. Li, and S. Chen, "Initial alignment by attitude estimation for strapdown inertial navigation systems," *IEEE Trans. Instrum. Meas.*, vol. 64, no. 3, pp. 784–994, Mar. 2015.
- [22] G. Wang, S. Qian, Q. Lv, H. Wei, H. Lin, and B. Liang, "UWB and IMU system fusion for indoor navigation," in *Proc. IEEE 37th Chin. Control Conf. (CCC)*, Jul. 2018, pp. 4946–4950.
- [23] A. Wang and Y. Song, "Improved SDS-TWR ranging technology in UWB positioning," in *Proc. IEEE Int. Conf. Sensor Netw. Signal Process. (SNSP)*, Oct. 2018, pp. 222–225.
- [24] A. Nouredin, T. B. Karamat, M. D. Eberts, and A. El-Shafie, "Performance enhancement of MEMS-based INS/GPS integration for low-cost navigation applications," *IEEE Trans. Veh. Technol.*, vol. 58, no. 3, pp. 1077–1096, Mar. 2009.
- [25] Y. Zhuang, Y. Li, L. Qi, H. Lan, J. Yang, and N. El-Sheimy, "A two-filter integration of MEMS sensors and WiFi fingerprinting for indoor positioning," *IEEE Sensors J.*, vol. 16, no. 13, pp. 5125–5126, Jul. 2016.
- [26] S. Wang, Y. Lyu, and W. Ren, "Unscented transformation based distributed nonlinear state estimation: Algorithm, analysis, and experiments," *IEEE Trans. Control Syst. Technol.*, vol. 27, no. 5, pp. 2016–2029, Sep. 2019.
- [27] E. A. Wan and R. Van Der Merwe, "The unscented Kalman filter for nonlinear estimation," in *Proc. IEEE Adapt. Syst. Signal Process. Commun. Control Symp. (ASSPCC)*, Oct. 2000, pp. 153–158.
- [28] C. Tang *et al.*, "Improvement of orbit determination accuracy for Beidou navigation satellite system with two-way satellite time frequency transfer," *Adv. Space Res.*, vol. 58, no. 7, pp. 1390–1400, May 2016.

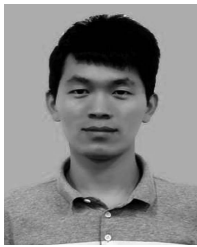


Daquan Feng received the Ph.D. degree in information engineering from the National Key Laboratory of Science and Technology on Communications, University of Electronic Science and Technology of China, Chengdu, China, in 2015.

He was a Research Staff with State Radio Monitoring Center, Beijing, China, and then a Postdoctoral Research Fellow with the Singapore University of Technology and Design, Singapore.

He was a visiting student with the School of Electrical and Computer Engineering, Georgia Institute of Technology, Atlanta, GA, USA, from 2011 to 2014. He is currently an Assistant Professor with the Guangdong Province Engineering Laboratory for Digital Creative Technology and Guangdong Key Laboratory of Intelligent Information Processing, College of Electronics and Information Engineering, Shenzhen University, Shenzhen, China. His research interests include URLLC communications, LTE-U, and massive IoT networks.

Dr. Feng is an Associate Editor of IEEE COMMUNICATIONS LETTERS and IEEE ACCESS.



Chunqi Wang received the B.S. degree in optoelectronics information science and engineering from the College of Testing and Opto-Electronic Engineering, Nanchang Hangkong University, Nanchang, China, in 2017. He is currently pursuing the master's degree in information and communication engineering with the Guangdong Province Engineering Laboratory for Digital Creative Technology and Guangdong Key Laboratory of Intelligent Information Processing, College of Electronics and Information Engineering, Shenzhen

University, Shenzhen, China.

His current research interests include pedestrians and robots positioning and navigation.

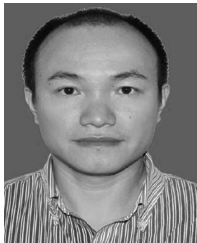


Yuan Zhuang (Member, IEEE) received the bachelor's degree in information engineering and the master's degree in microelectronics and solid-state electronics from Southeast University, Nanjing, China, in 2008 and 2011, respectively, and the Ph.D. degree in geomatics engineering from the University of Calgary, Calgary, AB, Canada, in 2015.

He was an Algorithm Designer with Trusted Positioning Inc., Calgary, and the Lead Scientist with Bluvision Inc., Fort Lauderdale, FL, USA. He is currently a Professor with the State Key Laboratory of

Information Engineering in Surveying, Mapping and Remote Sensing, Wuhan University, Wuhan, China. He has coauthored over 50 academic papers and 11 patents. His current research interests include multisensors integration, real-time location system, personal navigation system, wireless positioning, Internet of Things, and machine learning for navigation applications.

Prof. Zhuang has received over ten academic awards. He is an Associate Editor of IEEE ACCESS, the Guest Editor of the IEEE INTERNET OF THINGS JOURNAL and IEEE ACCESS, and a reviewer of over ten IEEE journals.



Chunlong He (Member, IEEE) received the M.S. degree in communication and information science from Southwest Jiaotong University, Chengdu, China, in 2010, and the Ph.D. degree from Southeast University, Nanjing, China, in 2014.

From September 2012 to September 2014, he was a visiting student with the School of Electrical and Computer Engineering, Georgia Institute of Technology, Atlanta, GA, USA. Since 2015, he has been with the College of Electronics and Information Engineering, Shenzhen University, Shenzhen, China,

where he is currently an Associate Professor. His research interests include communication and signal processing, green communication systems, channel estimation algorithms, and limited feedback techniques.

Dr. He is a member of the Institute of Electronics, Information, and Communication Engineering. He is currently an Associate Editor of IEEE ACCESS.



Xiang-Gen Xia (Fellow, IEEE) received the B.S. degree in mathematics from Nanjing Normal University, Nanjing, China, in 1983, the M.S. degree in mathematics from Nankai University, Tianjin, China, in 1986, and the Ph.D. degree in electrical engineering from the University of Southern California, Los Angeles, CA, USA, in 1992.

He was a Senior/Research Staff Member with Hughes Research Laboratories, Malibu, CA, USA, from 1995 to 1996. In September 1996, he joined the Department of Electrical and Computer Engineering,

University of Delaware, Newark, DE, USA, where he is the Charles Black Evans Professor. He has authored the book *Modulated Coding for Intersymbol Interference Channels* (New York: Marcel Dekker, 2000). His current research interests include space-time coding, MIMO and OFDM systems, digital signal processing, and SAR and ISAR imaging.

Dr. Xia received the National Science Foundation Faculty Early Career Development (CAREER) Program Award in 1997, the Office of Naval Research Young Investigator Award in 1998, and the Outstanding Overseas Young Investigator Award from the National Nature Science Foundation of China in 2001. He was the Technical Program Chair of the Signal Processing Symposium, Globecom 2007 in Washington, DC, USA, and the General Co-Chair of ICASSP 2005 in Philadelphia. He is currently serving/has served as an Associate Editor for numerous international journals, including the IEEE WIRELESS COMMUNICATIONS LETTERS, the IEEE TRANSACTIONS ON SIGNAL PROCESSING, the IEEE TRANSACTIONS ON WIRELESS COMMUNICATIONS, the IEEE TRANSACTIONS ON MOBILE COMPUTING, and the IEEE TRANSACTIONS ON VEHICULAR TECHNOLOGY.